CHEMISTRY OF MATERIALS

pubs.acs.org/cm

Article

Lead-Free Semiconductors: Phase-Evolution and Superior Stability of Multinary Tin Chalcohalides

Alison N. Roth, Andrew P. Porter, Sarah Horger, Kerly Ochoa-Romero, Gonzalo Guirado, Aaron J. Rossini, and Javier Vela*

Cite This: *Chem. Mater.* 2024, 36, 4542–4552

Read Online

ACCESS | Metrics & More | Article Recommendations | Supporting Information

ABSTRACT: Tin-based semiconductors are highly desirable materials for energy applications due to their low toxicity and biocompatibility relative to analogous lead-based semiconductors. In particular, tin-based chalcohalides possess optoelectronic properties that are ideal for photovoltaic and photocatalytic applications. In addition, they are believed to benefit from increased stability compared with halide perovskites. However, to fully realize their potential, it is first necessary to better understand and predict the synthesis and phase evolution of these complex materials. Here, we describe a versatile solution-phase method for the preparation of the multinary tin chalcohalide semiconductors $Sn_2SbS_2I_3$, $Sn_2BiS_2I_3$, Sn_2BiSI_5, and Sn_2SI_2. We demonstrate how certain thiocyanate precursors are selective toward the synthesis of chalcohalides, thus preventing the formation of binary and other lower order impurities rather than the preferred multinary compositions. Critically, we utilized ^{119}Sn ssNMR spectroscopy to further assess the phase purity of these materials. Further, we validate that the tin chalcohalides exhibit excellent water stability under ambient conditions, as well as remarkable resistance to heat over time compared to halide perovskites. Together, this work enables the isolation of lead-free, stable, direct band gap chalcohalide compositions that will help engineer more stable and biocompatible semiconductors and devices.

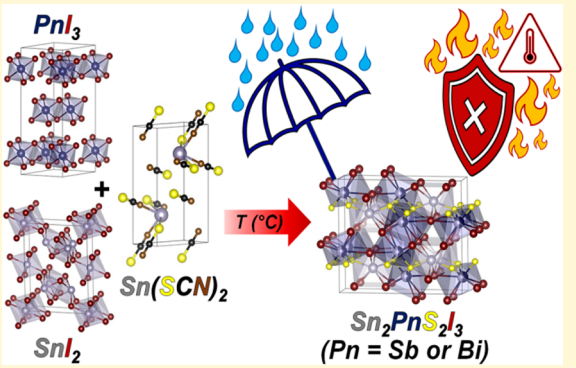

Semiconductors are ubiquitous optoelectronic materials that are critical to the functionality and efficiency of many existing technologies and devices. Their widespread use and our reliance on semiconductors for many new emerging technologies make it especially important to focus on materials and compositions that demonstrate enhanced stability and biocompatibility. For instance, while lead halide perovskites are increasingly used in photovoltaic, catalytic, and light-emitting devices (LEDs), they are often based on a toxic element (Pb), and suffer from water-, thermal-, and photoinduced phase segregation and degradation.[1,2] Combined, these problems result in significant environmental and technological challenges that can hinder device performance and significantly slow down the deployment of new technologies.[3−5]

In the search for alternatives, chalcohalides are quickly gaining attention as semiconductors for multiple applications.[6−13] For example, quaternary lead-free $Sn_2PnS_2I_3$ (where Pn = Sb or Bi) chalcohalides display some of the most desirable features of chalcogenide and halide materials, including direct, visible band gaps (<1.6 eV).[14−19] Following their original discovery and crystallographic determination, these materials have earned renewed interest in photovoltaics, thermoelectrics, and catalysis applications.[20−24] Furthermore, based on preliminary solar devices, tin chalcohalides are believed to exhibit inherently high stability and power conversion efficiency (PCEs), highlighting their potential as valuable materials for energy conversion.[25,26]

Typically, chalcohalide single crystals are grown after direct solid-state reaction between the elements (Figure 1).[27−29] However, aside from the preparation of $Sn_2SbS_2I_3$ thin-films employing a high temperature annealing approach,[25] the solution-phase synthesis of tin-based chalcohalides remains relatively unexplored.[30] Moreover, while the colloidal synthesis of bismuth-based, ternary chalcohalides such as BiSI and $Bi_{13}S_{18}I_2$ has undergone a renaissance in the past few years,[31−37] surprisingly little synthetic attention has been paid to tin-based, ternary chalcohalides such as Sn_2SI_2.[38−40]

Inspired by recent work on the solution-phase synthesis of lead-based chalcohalides, we hypothesized that the solution-phase synthesis of both quaternary and ternary Sn chalcohalides could be attained using thiocyanate precursors. Thiocyanates have proven to be useful in the preparation of

Received: January 24, 2024
Revised: March 21, 2024
Accepted: March 22, 2024
Published: April 19, 2024

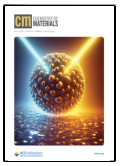

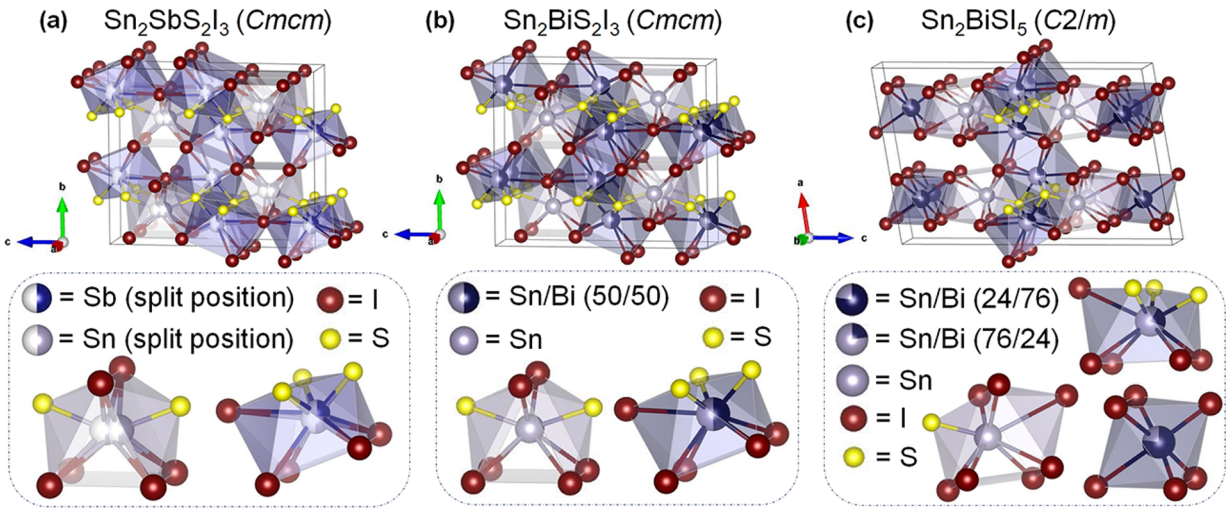

Figure 1. Unit cells of quaternary tin chalcohalides: (a) *Cmcm* $Sn_2SbS_2I_3$, (b) *Cmcm* $Sn_2BiS_2I_3$, and (c) *C*2/*m* Sn_2BiSI_5. (Note: $Sn_2SbS_2I_3$ displays both compositional and positional disorder with Sn and Sb,[21] while $Sn_2BiS_2I_3$ and Sn_2BiSI_5 display only compositional disorder with mixed occupancy sites of Sn and Bi.[17])

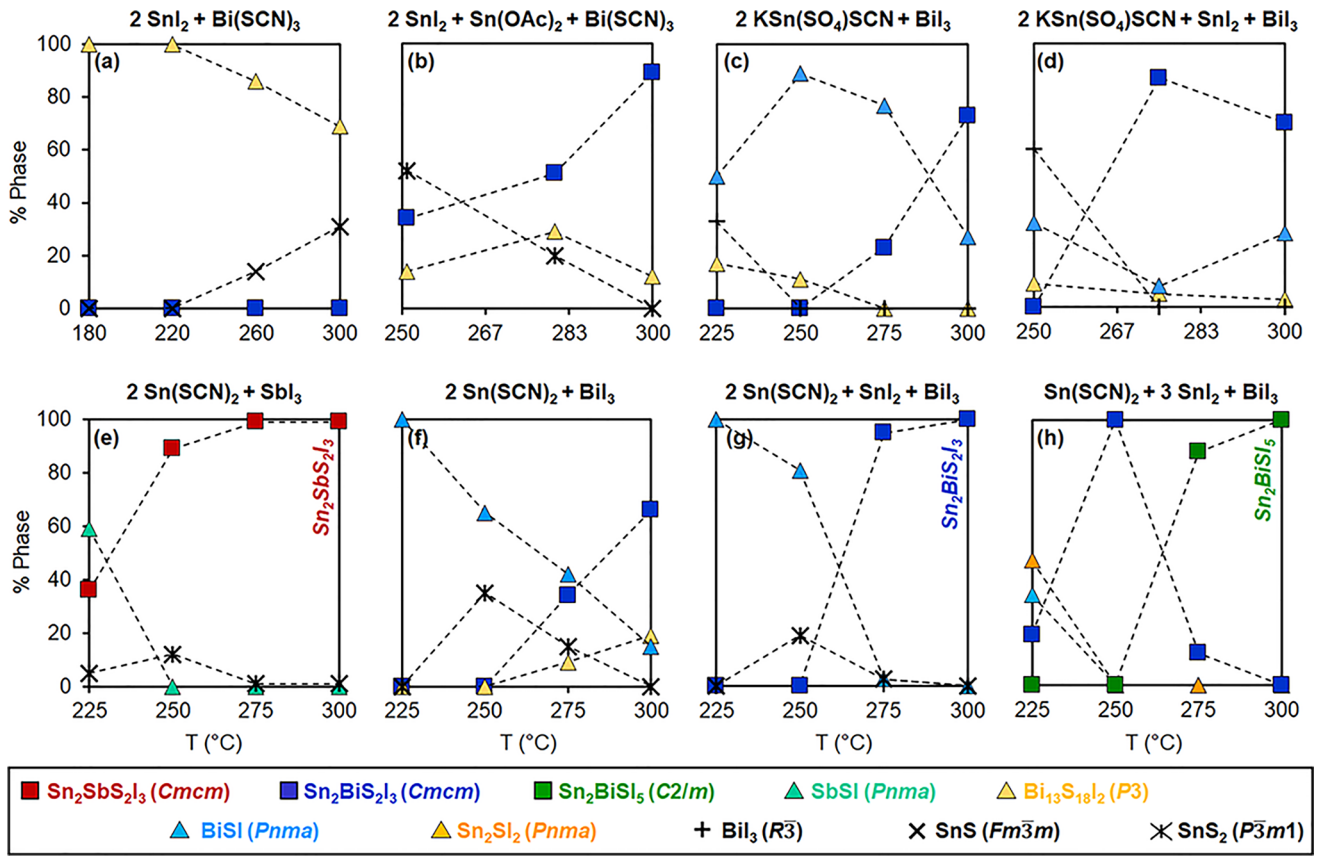

Figure 2. Phase evolution of quaternary (□) and ternary (△) tin chalcohalides using thiocyanate, halide, and acetate precursors under comparable reaction conditions (20−60 mM SCN precursor, 10 mL of ODE + oleic acid; see the Experimental Section).

both chalcogenides[41] and chalcohalides[42−44] due to the presence of a preformed metal−sulfur bond, which aids in controlling particle nucleation and growth.[43,44] However, even with this particular chemical strategy in hand, the synthetic phase space in which multinary chalcohalides form at relatively low temperatures (<300 °C) from solution is expected to be complex due to numerous competing binary, ternary, and quaternary phases. Consequently, difficulties often arise in isolating the specific multinary compositions unless their phase evolution is thoroughly understood.

In this study, we examine the phase-specific synthesis of the quaternary and ternary tin chalcohalides $Sn_2SbS_2I_3$, $Sn_2BiS_2I_3$, Sn_2BiSI_5, and Sn_2SI_2. We demonstrate that using different types of thiocyanate precursors affects their formation as well as the presence of lower order impurities. We employ ^{119}Sn solid-state (ss) NMR spectroscopy to probe the local Sn environment in each semiconductor and further assess their

https://doi.org/10.1021/acs.chemmater.4c00209
Chem. Mater. 2024, 36, 4542−4552

phase purity. Importantly, experiments demonstrate that chalcohalides have excellent thermal and moisture stability compared to standard halide perovskites, further highlighting their suitability for device applications.

RESULTS AND DISCUSSION

Precursor Screening: Where Thiocyanate Matters. Precursor selection is key to achieving phase and shape selectivity as well controlling particle size in solution.[45−49] Successful synthesis requires precursors and conditions that favor the nucleation and growth of the desired, multinary phase, often in a series of multiple steps,[50−54] while suppressing the nucleation and preventing the runaway growth of competing binaries or lower order phases and impurities. With this in mind, we resorted to metal thiocyanates as precursors to simultaneously introduce the desired Sn, Pn (Sb or Bi) and S elements. We specifically investigated supplying the thiocyanate along with the pnictide ($Bi(SCN)_3$[55]) or tin ($KSn(SO_4)SCN$[56] or $Sn(SCN)_2$[57]) precursors, with initial concentrations of 20−60 mM in a 10 mL mixture of 1-octadecene (ODE) and oleic acid (see the Experimental Section).

Powder X-ray diffraction (XRD) of the solids isolated from the reaction of $Bi(SCN)_3$ with SnI_2 across a wide temperature range consist of ternary $Bi_{13}S_{18}I_2$,[31,32] without evidence for quaternary formation (Figure 2a); see Supporting Information available (SI). Given that SnI_2 appears to insufficiently deliver tin to the medium, we introduced tin acetate ($Sn(OAc)_2$) as an additional tin precursor. This approach succeeds in producing $Sn_2BiS_2I_3$ at 300 °C, although ca. 10% of the crystalline solids are still made of $Bi_{13}S_{18}I_2$ (Figure 2b). Prolonged reaction times at 300 °C failed to increase the yield of $Sn_2BiS_2I_3$; instead, the quaternary atom is quickly replaced by $Bi_{13}S_{18}I_2$ and, eventually, Bi metal. Therefore, while $Bi(SCN)_3$ serves as a precursor to quaternary, $Bi_{13}S_{18}I_2$ impurities are difficult to avoid. Because of this and given the limited availability of $Sb(SCN)_3$, we decided to investigate supplying the thiocyanate with the tin precursor.

Reaction of $KSn(SO_4)SCN$[56] with SbI_3 results in $Sn_2SbS_2I_3$ that is free of crystalline impurities. However, scanning electron microscopy (SEM) and energy dispersive spectroscopy (EDS) reveal that a significant amount of amorphous K_2S is present throughout the sample (see the SI). This impurity, which is hard to detect by powder XRD alone, originates from the potassium-containing thiocyanate precursor. Interestingly, the reaction of $KSn(SO_4)SCN$ with BiI_3 gradually produces the ternary bismuth chalcohalides BiSI and $Bi_{13}S_{18}I_2$ and, above 275 °C, quaternary $Sn_2BiS_2I_3$ (Figure 2c). However, a significant amount of BiSI is still present at 300 °C, even when SnI_2 is introduced as an additional tin precursor (Figure 2d). Therefore, while promising, $KSn(SO_4)SCN$ has limitations as a suitable precursor for synthesizing quaternary chalcohalides.

By contrast to the aforementioned results, reaction of $Sn(SCN)_2$[57] with SbI_3 initially forms a mixture of binary, ternary, and quaternary phases below 250 °C, but cleanly transforms into phase pure $Sn_2SbS_2I_3$ (*Cmcm*) at 300 °C (Scheme 1 and Figure 2e). Similarly, the reaction between $Sn(SCN)_2$ and BiI_3 initially forms a mixture of BiSI and SnS_2, which then transforms into $Sn_2BiS_2I_3$—albeit, some $Bi_{13}S_{18}I_2$ forms above 275 °C (Figure 2f). Interestingly, using both $Sn(SCN)_2$ and SnI_2 along with BiI_3 enables the preparation of phase-pure $Sn_2BiS_2I_3$ (*Cmcm*) (Figure 2g). Rietveld refined XRD patterns agree well with their respective quaternary compositions and further support their phase purity (see the SI).

Scheme 1. Solution-Phase Synthesis of Tin-Based, Quaternary $Sn_2PnS_2I_3$ Chalcohalides (Pn = Sb or Bi)

$$2Sn(SCN)_2 + PnI_3 + 6O_2 \xrightarrow[\text{ODE, oleic acid}]{\text{300 °C, 30 s}} Sn_2PnS_2I_3 + 2SO_2 + 4CO_2 + 2N_2$$

Pn = Sb or Bi

Synthesis of Iodine-Rich Quaternary Sn_2BiSI_5. Further increasing the initial concentration of SnI_2 (20 mM) by two or three enables the preparation of a different, iodine-rich quaternary Sn_2BiSI_5 (*C*2/*m*) phase (Figure 2h). Increasing the oleic acid concentration to 2.5 M further facilitates the isolation of this different quaternary (Scheme 2), which may be attributed to increased solubility of SnI_2 in oleic acid (see the Experimental Section and SI).

Scheme 2. Solution-Phase Synthesis of Additional Tin-Based, Quaternary Sn_2BiSI_5 and Ternary Sn_2SI_2 Chalcohalides (not balanced)

(a)

$$Sn(SCN)_2 + xSnI_2 + BiI_3 + 3O_2 \xrightarrow[\text{300 °C, 30 s}]{\text{ODE, oleic acid}} Sn_2BiSI_5 + SO_2 + 2CO_2 + N_2$$

x = 2 or 3

(b)

$$Sn(SCN)_2 + xSnI_2 + 3O_2 \xrightarrow[\text{300 °C, 30 s}]{\text{ODE, oleic acid}} Sn_2SI_2 + SO_2 + 2CO_2 + N_2$$

x = 1, 2, or 3

To further evaluate the importance of the thiocyanate precursor, we attempted to synthesize quaternary chalcohalides using a combination of metal carboxylates, elemental sulfur, and oleylammonium iodide ($oleylNH_3^+I^-$, sometimes also referred to as "I-OLAM").[58] Using the synthesis of $Sn_2BiS_2I_3$ as a test bed, we find that tin- and bismuth-carboxylates produce a mixture of $Bi_{13}S_{18}I_2$ and SnS (see the SI). Using bismuth carboxylates and elemental sulfur while also introducing the more reactive SnI_2 instead of $oleylNH_3^+I^-$ results in more quaternary formation, yet binary SnS or SnS_2 impurities persist. These results further demonstrate that a combined thiocyanate/metal halide approach is among the most effective for synthesizing quaternary tin chalcohalide semiconductors.

SEM imaging shows that $Sn_2SbS_2I_3$, $Sn_2BiS_2I_3$, and Sn_2BiSI_5 adopt highly anisotropic morphologies with high aspect ratios (l/w), such as rods and needles, such as those observed for their lead-based analogues (Figure 3).[43] The average rod widths range from ca. 700 nm to 2 μm, while the rod lengths range from 5 to 15 μm. EDS confirms the elemental composition of the phase-pure tin chalcohalides (Figure 3 and Table 1).

Molecular Basis for Phase Selectivity. A possible explanation for the relative reactivity and phase selectivity observed is based on the stability of the different metal−sulfur and metal-halide bonds that are present in the different molecular precursors.[59] The strongest among these is the Sn−S bond at 464 kJ/mol, followed by Sb−S and Bi−S bonds at 379 and 316 kJ/mol, respectively.[59] Stronger bonds are harder to make and harder to break, because both M−S bond forming and breaking processes involve a higher energy of activation.[60]

Indeed, our data show that to form quaternary tin chalcohalides, it is best to employ a precursor that already

https://doi.org/10.1021/acs.chemmater.4c00209
Chem. Mater. 2024, 36, 4542−4552

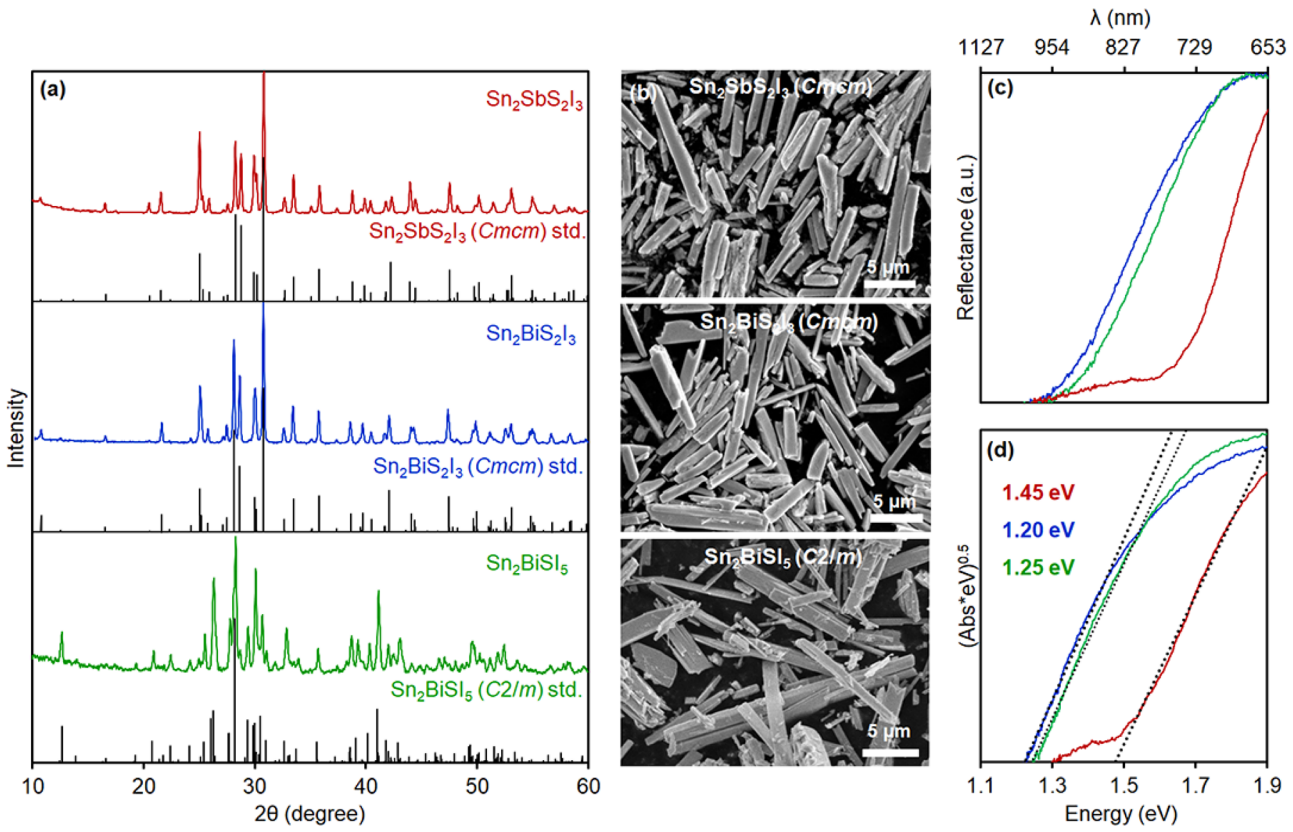

Figure 3. Powder XRD patterns (a), SEM images (b), diffuse reflectance spectra (c), and direct band Tauc plots (d) of $Sn_2SbS_2I_3$, $Sn_2BiS_2I_3$, and Sn_2BiSI_5 (20−60 mM SCN precursor, 10 mL of ODE + oleic acid; see the Experimental Section).

Table 1. Synthesis of Quaternary and Ternary Tin Chalcohalides[a,b]

Sn prec(s). (mmol)	Pn prec. (mmol)	ligands/solvents[a] (mL)	product[c] (EDS)[d]	Exp. gap Abs, CV/eV (nm)	width(w, μm)	length[d] (l, μm)	aspect ratio (l/w)
$Sn(SCN)_2$ (0.4)	SbI_3 (0.2)	ODE (8) OA (2)	*Cmcm* $Sn_2SbS_2I_3$ ($Sn_{1.9}SbS_{2.0}I_{3.1}$)	1.45 (855), 1.55	1.5 ± 0.5	9.7 ± 2.5	6
$Sn(SCN)_2$ (0.4) SnI_2 (0.2)	BiI_3 (0.2)	ODE (8) OA (2)	*Cmcm* $Sn_2BiS_2I_3$ ($Sn_{2.0}BiS_{1.8}I_{2.9}$)	1.20 (1033), 1.32	0.7 ± 0.2	6.7 ± 2.1	10
$Sn(SCN)_2$ (0.2) SnI_2 (0.6)	BiI_3 (0.2)	ODE (2) OA (8)	*C2/m* Sn_2BiSI_5 ($Sn_{2.1}BiS_{1.1}I_{4.8}$)	1.25 (992), 1.25	1.2 ± 0.4	14 ± 6.0	12
$Sn(SCN)_2$ (0.2) SnI_2 (0.2)	none	ODE (8) OA (2)	*Pnma* Sn_2SI_2 ($Sn_{1.7}SI_{1.5}$)	2.11 (588)	0.68 ± 0.15	17.5 ± 6.1	25
$Sn(SCN)_2$ (0.2) SnI_2 (0.4)	none	ODE (8) OA (2)	*Pnma* Sn_2SI_2 ($Sn_{2.1}SI_{2.1}$)	2.03 (605), 1.97	1.3 ± 0.33	19 ± 6.4	15
$Sn(SCN)_2$ (0.2) SnI_2 (0.6)	none	ODE (8) OA (2)	*Pnma* Sn_2SI_2 ($Sn_{2.5}SI_{2.7}$)	1.92 (646)	3.2 ± 1.1	14 ± 4.6	4
$Sn(SCN)_2$ (0.2) SnI_2 (0.8)	none	ODE (2) OA (8)	91% *C2/m* Sn_2SI_2 9% *Pnma* Sn_2SI_2	1.96 (633)	2.5 ± 1.1	15 ± 4.7	6

[a]General conditions: T = 300 °C, t = 30 s. [b]Total reaction volume = 10 mL. [c]From Match! [d]From SEM (see the Experimental Section).

contains preformed Sn−S bonds and can deliver premade [SnS] building blocks to the reaction, such as $Sn(SCN)_2$. Instead, only ternary bismuth chalcohalides form when $Bi(SCN)_3$ is used. In comparison to M−S bonds, M-halide (M-X) bonds are relatively weak at Sn−I and Bi−I at 235 and 186 kJ/mol, respectively. Metal-halide bonds are relatively easy to make and break; thus, a variety of M−I precursors are able to provide $I(SnI)_n$ (n = 0 (I^-), 1, 2···) building blocks to cap and link [SnS] units during nucleation and growth.

Solution-Grown Ternary Tin Chalcohalides. Our synthetic approach succeeds in the preparation of ternary chalcohalides as well. Valuable targets include tin-based ternary chalcohalides which previously lacked a reported solution-phase synthesis.[38−40] Phase pure, orthorhombic (*Pnma*) Sn_2SI_2 forms at 300 °C by reacting together 20 mM $Sn(SCN)_2$ with a 1-to-3-fold excess of added SnI_2 (Scheme 2 and Figure 4). Interestingly, during synthetic optimization we observed the disordered monoclinic (*C2/m*) Sn_2SI_2 polymorph in a highly concentrated (2.5 M) oleic acid solution with a 4-fold excess of SnI_2. XRD showed mostly *C2/m* Sn_2SI_2 (91%) with a small amount of the orthorhombic (*Pnma*) polymorph (Table 1; see the SI).

This finding is unexpected because a higher SnI_2 concentration continues to favor the formation of Sn_2SI_2

https://doi.org/10.1021/acs.chemmater.4c00209
Chem. Mater. 2024, 36, 4542−4552

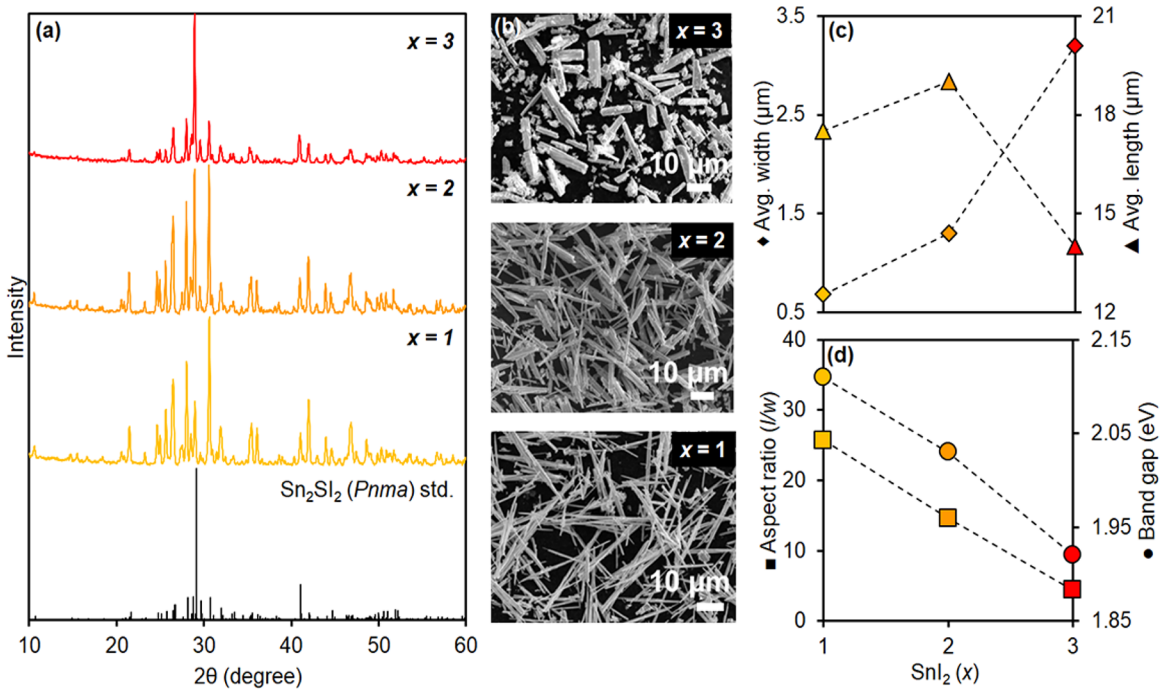

Figure 4. Powder XRD patterns (a), SEM images (b), particle dimensions (c), and band gap to aspect ratio comparison (d) of solution-grown *Pnma* Sn_2SI_2 (20−80 mM Sn, 10 mL ODE + oleic acid; see the Experimental Section).

polymorphs rather than the more iodine-rich composition Sn_4SI_6 ($C2/m$). SEM-EDS shows that the Sn_2SI_2 polymorphs adopt rod-like morphologies. Interestingly, the aspect ratio (l/w) of the particles decreases from ∼25 to ∼4 when the concentration of SnI_2 precursor used increases from one- to 3-fold (20 to 60 mM) relative to that of $Sn(SCN)_2$ (20 mM) (Figure 4). This coincides with a slight increase in the iodine content compared with the theoretical ternary stoichiometry and demonstrates a possible entry for controlling the particle size and tuning the optoelectronic properties of Sn_2SI_2 and other chalcohalides.

Optoelectronic Characterization. Previous studies indicate that $Sn_2PnS_2I_3$ (Pn = Sb, Bi) chalcohalides are direct band gap semiconductors. Here, we evaluated the solution-grown materials optically via diffuse reflectance spectroscopy and electrochemically using cyclic voltammetry. Direct gap Tauc plots[61] derived from the diffuse reflectance spectra yield 1.45 eV (855 nm), 1.20 eV (992 nm), and 1.25 eV (1033 nm) gaps for $Sn_2SbS_2I_3$, $Sn_2BiS_2I_3$, and Sn_2BiSI_5, respectively (Figure 3). These values closely agree with other experimental and calculated values and further support the suitability of these materials as semiconductors for light harvesting devices.[17]

Unlike its quaternary counterparts, Sn_2SI_2 is predicted to be an indirect band gap semiconductor.[38,39] Diffuse reflectance measurements reveal a band of 1.96 eV (633 nm) for the monoclinic ($C2/m$) Sn_2SI_2 polymorph (see the SI). For the orthorhombic (*Pnma*) polymorph, the band gap gradually red shifts from 2.11 to 1.92 eV (588−646 nm) as the concentration of SnI_2 used in the synthesis increases (Figure 4). This change in optical properties is directly proportional to the decreasing aspect ratio (l/w) of the Sn_2SI_2 particles observed from SEM. However, it is unlikely that this phenomenon is related to quantum confinement effects due to the large particle dimensions. Nonetheless, this shows that it is still possible to synthetically tune both the particle size and the optical properties of Sn_2SI_2.

Cyclic voltammograms (CVs) were obtained for the quaternary and ternary Sn chalcohalides to better assess their electronic band alignment in addition to their band gap energies. The anodic (E_{pa}) and cathodic (E_{pc}) peak potential values were derived from well-defined oxidation (E_{ox}) and reduction (E_{red}) waves in the CV (with respect to a saturated calomel electrode), and used to extrapolate the HOMO−LUMO energies using relationships:

$$E(\text{HOMO}) = -I_p = -(E_{ox} + 4.20)\text{eV}$$

$$E(\text{LUMO}) = -E_a = -(E_{red} + 4.20)\text{eV}$$

The electrochemically determined ionization potentials (I_p) and electron affinities (E_a) for the tin chalcohalides reveal narrowing band gap values from 1.97 to 1.55, 1.32, and 1.25 eV for Sn_2SI_2, $Sn_2SbS_2I_3$, $Sn_2BiS_2I_3$, and Sn_2BiSI_5, respectively (Figure 5). These values agree well with those obtained from diffuse reflectance and are consistent with general trends in the lead chalcohalide series.[43]

^{119}Sn ssNMR Spectroscopy. To investigate the local environment of Sn, we employed direct excitation ^{119}Sn solid-state NMR spectroscopy. ^{119}Sn is a spin 1/2 nucleus that has a natural isotopic abundance of 8.6% and is known to possess an isotropic chemical shift range of 1000 ppm to −2000 ppm for diamagnetic compounds, making ^{119}Sn NMR spectra extremely sensitive to changes in Sn local environment.[62] First, we collected ^{119}Sn NMR spectra of precursors $Sn(SCN)_2$ and $KSn(SO_4)(SCN)$ (see the SI). These spectra exhibit narrow peaks and shows isotropic chemical shift of −812 and −978 ppm, respectively. Neither peak is observed in the NMR spectra of the Sn chalcohalides, indicating that the reactants are fully consumed and converted to other products.

All of the tin iodide materials studied here give rise to broad ^{119}Sn NMR signals. For comparison, quaternary lead

https://doi.org/10.1021/acs.chemmater.4c00209
Chem. Mater. 2024, 36, 4542−4552

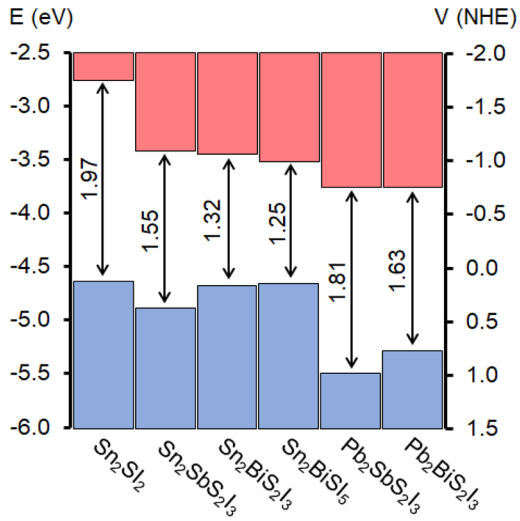

Figure 5. Electrochemically determined band energy levels and alignment of tin and lead[43] chalcohalide semiconductors (see the Experimental Section).

chalcohalides containing mixed-halides (i.e., Pb_3SBrI_3) also exhibit a single broad ^{207}Pb ssNMR signal despite having multiple Pb environments in their structure.[44] In a previous study of ^{119}Sn solid-state NMR spectra of mixed halide Sn perovskites, the compound perovskite methylammonium tin iodide ($CH_3NH_3SnI_3$) showed a broad ^{119}Sn NMR signal with a peak width of ca. 26 kHz.[63] We observe similarly broadened ^{119}Sn NMR spectra here (Figure 6), with peak widths on the order of ca. 70 kHz at 9.4 T and ca. 100 kHz at 14.1 T—the origin of the broadening is further discussed below. During synthetic development, a common amorphous impurity that was observed by ^{119}Sn NMR—but not by powder XRD—was SnS_2.[64]

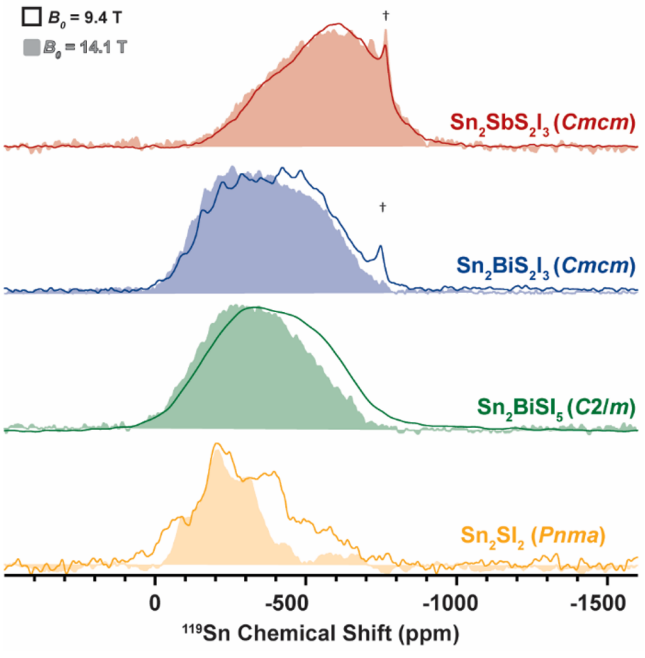

Figure 6. ^{119}Sn spin echo solid-state NMR spectra of $Sn_2SbS_2I_3$, $Sn_2BiS_2I_3$, Sn_2BiSI_5, and Sn_2SI_2 at 9.4 T (lines) and 14.1 T (shaded). 9.4 T NMR spectra were collected using an MAS frequency of 12.5 kHz for $Sn_2SbS_2I_3$, $Sn_2BiS_2I_3$, and Sn_2BiSI_5. Spectra collected at 14.1 T were measured with a 10 kHz MAS spinning frequency. A 25 kHz MAS frequency was used for Sn_2SI_2 at both fields. († indicates a possible SnS_2 impurity at −762 ppm.[64])

The simplest compound studied here, $Sn_2SbS_2I_3$, gives rise to a ^{119}Sn NMR signal that was 65 kHz broad at 9.4 T, despite the fact that only a single Sn site was reported in the original crystal structure of this material.[28] A comparison of the ^{119}Sn NMR spectra of $Sn_2SbS_2I_3$ obtained at 9.4 and 14.1 T shows that the spectra are similar in appearance when plotted in units of ppm. This observation suggests that the broadening of the ^{119}Sn NMR spectrum is primarily inhomogeneous. Inhomogeneous broadening occurs from structural disorder that leads to a distribution in the isotropic chemical shift and/or from the effects of chemical shift anisotropy (CSA). Fitting the ^{119}Sn NMR spectra of $Sn_2SbS_2I_3$ to a single Sn site suggests the span (Ω) is ca. 360 ppm and the δ_{iso} value is −547 ppm. To fit the spectrum to a single Sn site, we used Gaussian line broadening of 29 kHz and 46 kHz at 9.4 T and 14.1 T, respectively, corresponding to 194 ppm of inhomogeneous broadening. If the span is 360 ppm, the fits suggest that part of the ^{119}Sn NMR spectrum could correspond to spinning sidebands. The fit suggests that the true isotropic chemical shift is *ca.* − 547 ppm with an isotropic shift distribution of approximately ±200 ppm. We also attempted a two-site fit of the spectrum. The two-site fit yielded isotropic chemical shifts of −417 ppm and −630 ppm, again, with sizable shift distributions on the order of 200 ppm.

For all fits, we used a constant Lorentzian broadening of 5 kHz (see the SI). The amount of Lorentzian broadening used in the fit was estimated from measuring the homogeneous ^{119}Sn transverse relaxation time constant (T_2') at 9.4 T, which suggested T_2' was less than 300 μs. Similarly short T_2' are observed for the other Sn compounds. The homogeneous broadening likely occurs because of the dipolar and scalar coupling between ^{119}Sn and ^{127}I. ^{127}I is a spin $^5/_2$ quadrupolar nucleus that is 100% naturally abundant. It has been shown before that when ^{119}Sn or ^{207}Pb are dipole and/or scalar coupled to an abundant quadrupolar nucleus such as ^{127}I, there can be efficient transverse and longitudinal relaxation.[63,65,66] The efficient relaxation of the spin 1/2 nucleus occurs because some combination of rapid longitudinal relaxation of the quadrupolar nucleus or chemical exchange (diffusion) of the iodide anions.[44,63,64,66]

Thus, acquisition of the ^{119}Sn NMR spectra of $Sn_2SbS_2I_3$ at 9.4 and 14.1 T and simulations suggest that the NMR spectrum of $Sn_2SbS_2I_3$ is primarily inhomogeneously broadened due to an isotropic chemical shift distribution and partly due to CSA and spinning sideband overlap. The observed inhomogeneous broadening is consistent with the presence of significant structural disorder, giving support to recent crystallographic models of $Sn_2SbS_2I_3$ which exhibit multiple S and I positions as well as Sn and Sb site mixing.[21]

Moving down to the heavier pnictide (Pn), the crystal structure of $Sn_2BiS_2I_3$ shows two unique Sn sites, one of which exhibits mixed Pn occupancy (50% Sn:50% Bi). Similar ^{119}Sn NMR line widths were observed for $Sn_2SbS_2I_3$ and $Sn_2BiS_2I_3$. The inhomogeneous broadening persists in the ^{119}Sn NMR spectrum of Sn_2BiSI_5, which contains the largest number of Sn sites, including two mixed occupancy sites (24% Sn:76% Bi and 76% Sn:24% Bi). For Sn_2BiSI_5, the peak width was approximately 75 kHz at 9.4 T.

https://doi.org/10.1021/acs.chemmater.4c00209
Chem. Mater. 2024, 36, 4542−4552

Considering the literature on tin halide perovskites and related phases,[63] perovskites generally show more positively shifted ^{119}Sn NMR signals as the amount of iodine in the lattice was increased. A similar trend is observed here, where the more iodine rich phases tend to exhibit ^{119}Sn NMR signals shifted to higher (more positive) frequencies.

The ^{119}Sn NMR spectrum of Sn_2SI_2 gives rise to narrower NMR signals. In this compound, the ^{119}Sn T_1 is approximately four times longer (T_1 = 30 s) than the ^{119}Sn T_1 of the other compounds (T_1 = 8 s), suggesting that relaxation due to coupling with ^{127}I is not as efficient. The 14.1 T ^{119}Sn NMR spectrum of Sn_2SI_2 shows narrowing (when plotted in parts per million) as compared to the 9.4 T spectrum. This observation suggests that the broadening of the ^{119}Sn NMR spectra is primarily homogeneous in nature. Compared to the aforementioned, pnictide-containing quaternary compositions, which show either positional or compositional disorder (or even a combination of the two), *Pnma* Sn_2SI_2 is completely ordered, with six different Sn sites.[39] Three of these Sn sites show coordination environments of SnS_3I_5, while the remaining sites adopt coordination environments of $SnSI_5$, $SnSI_7$, and $SnSI_6$, respectively (see the SI). Interestingly, only three, significantly less broad, NMR peaks are present in the NMR spectrum, suggesting that Sn_2SI_2 is more crystalline than other tin chalcohalides.

Superior Moisture and Thermal Stability. To better assess the durability of tin-based chalcohalides for various electronic applications, we exposed them to excess water and compared their moisture stability to freshly made samples of halide perovskites as reference materials.[67,68] Briefly, we vigorously stirred each chalcohalide or perovskite sample in water for 2 days (48 h). Remarkably, powder XRD of the tin chalcohalides lacks any signs of degradation or formation of crystalline impurities after exposure to water (Figure 7). In contrast, both tin- and lead-based halide perovskites show major signs of decomposition after the same water treatment. Specifically, $CsPbI_3$ decomposes to PbI_2 over 48 h, while $CsSnI_3$ visibly decomposes to a completely amorphous, white product within the first 1 h in water. This highlights a potential challenge with other tin-based semiconductors, such as tin halide perovskites, which are susceptible to moisture-induced decomposition through the oxidation of Sn^{2+} to Sn^{4+}.[76]

To better assess the possibility of tin oxidation in the chalcohalides, we performed X-ray photoelectron spectroscopy (XPS) on $Sn_2SbS_2I_3$ before and after water exposure (see the SI). Looking first at the Sn 3d region, we observe a small shift in the Sn $3d_{5/2}$ binding energy from 486.4 to 486.6 eV after exposure to water. While these binding energies are not too far from those reported for SnS_2 ($3d_{5/2}$ = 486.8 eV) and SnO ($3d_{5/2}$ = 486.1 eV),[69] it is difficult to identify the chemical state of Sn from this region alone. Therefore, we also evaluated the Sn MNN Auger region, which yielded modified Auger parameters of 921.5 and 921.1 eV for the freshly prepared sample and the water treated sample, respectively. These values suggest that the chemical states of Sn in both samples are closer to those of metallic Sn (922.3 eV) and Sn^{2+} (919.7 eV) rather than Sn^{4+} (919.0 eV). For comparison, SnS and SnO_2 have modified Auger parameters of 921.3 and 919.2 eV, respectively.[69] Despite overlap of the Sb 3d and O 1s regions, a slightly larger O 1s component after exposure to water may suggest either more adsorbed water (or surface oxides) on the surface of the water treated sample. Considering all of the data, we conclude that even though there are surface oxide species present on $Sn_2SbS_2I_3$, the chemical state of Sn remains closer to 2+ rather than 4+, and that this is relatively unaffected by exposure to water.

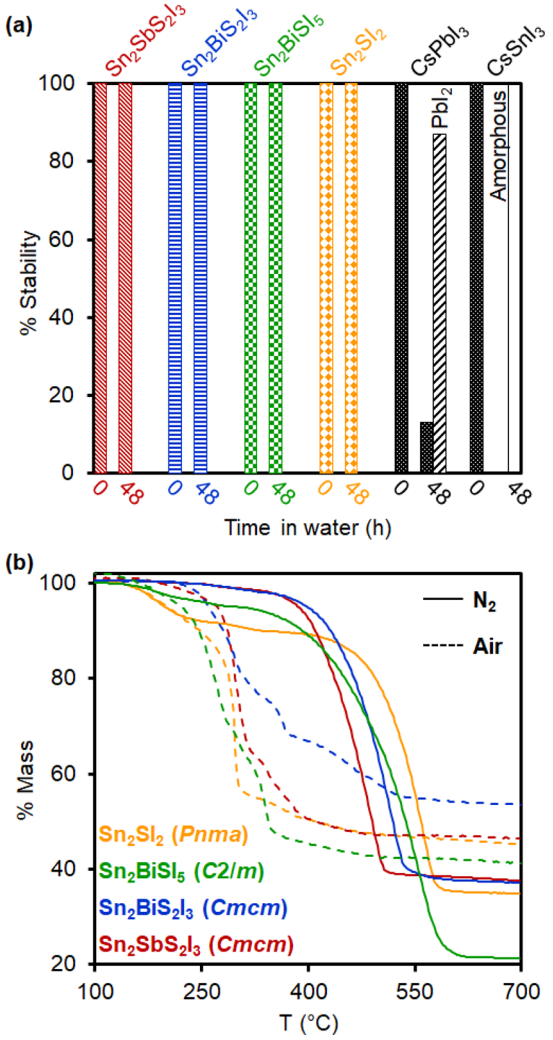

Figure 7. (a) Stability of tin chalcohalides stirred in water for 48 h (21 °C) compared to $CsSnI_3$ and $CsPbI_3$ perovskites.[67,68] (b) TGA analysis of tin chalcohalides under N_2 (solid line) or in air (dashed).

Finally, we studied the thermal stability of the tin chalcohalides using thermogravimetric analysis (TGA) and differential scanning calorimetry (DSC) under different environments. Under an inert (N_2) atmosphere, the onset of decomposition for all materials occurs between 400−450 °C (Figure 7). Among the quaternaries, general stability appears to increase with increasing formula weight, specifically on going from $Sn_2SbS_2I_3$ to the heavier pnictide-containing quaternary compositions $Sn_2BiS_2I_3$ and Sn_2BiSI_5. Notably, ternary Sn_2SI_2 exhibits a decomposition onset around 500 °C, the highest out of the tin chalcohalide series in our study. Under air, the thermal decomposition of the chalcohalides occurs at slightly lower temperatures, with mass loss beginning around 250 °C. These data are strikingly different from the thermal profile of halide perovskites: While there are a number of factors that influence their thermal stability—i.e., cation- and halide-composition, particle size, surface treatment, etc.—many halide perovskites decompose between 200 and 400 °C under an inert atmosphere,[70−75] and as low as 180 °C under air.[76] Therefore, combined with their superior moisture

https://doi.org/10.1021/acs.chemmater.4c00209
Chem. Mater. 2024, 36, 4542−4552

stability mentioned above, tin chalcohalides are a much more robust and stable alternative to perovskites as materials for energy conversion and catalytic devices.

CONCLUSIONS

This work advances the fundamental synthetic chemistry of lead-free chalcohalides starting from readily available and air-stable precursors and conditions. Understanding the complex phase space associated with quaternary compositions reveals optimal conditions to prepare specific chalcohalides, while avoiding impurities. Despite the fact that each of the thiocyanate precursors tested provides a source of sulfur and a cation (Sn or Sb/Bi), each elicits the phase evolution of various binary, ternary, and quaternary products. The formation of each quaternary chalcohalide is often preceded by the formation of lower order binary and ternary products. ^{119}Sn ssNMR helps distinguish between different quaternary chalcohalide phases and detect trace amounts of amorphous impurities that are otherwise silent by XRD or hard to detect by SEM-EDS. In addition to their direct optical band gap character, the chalcohalides display great resilience to moisture and heat, which is favorable for semiconductors intended for numerous applications, including photovoltaics, thermoelectrics, and catalysis.

Future studies will expand upon this knowledge to synthesize colloidal nanoscale versions of these materials that are more conducive to thin film deposition and device fabrication. Additionally, other multinary tin chalcohalide compositions such as $Sn_7Br_{10}S_2$ and $CdSnSX_2$ (X = Cl or Br) exhibit properties that are highly suitable for either nonlinear optics (NLO)[77] or photocatalysis,[78] respectively, and their colloidal chemistry remains underexplored. Additionally, halide-mixing and chalcogen-mixing are yet to be studied in tin chalcohalides, potentially offering a wider range of compositional, structural, and optical tunability for a variety of applications.[16]

EXPERIMENTAL SECTION

Materials. 1-Octadecene (ODE, technical grade, 90%), potassium thiocyanate (KSCN, 99%) sodium thiocyanate (NaSCN, 98%), and tin(II) acetate ($Sn(OAc)_2$) from Sigma-Aldrich; antimony(III) iodide (SbI_3, 99.9%), bismuth(III) iodide (BiI_3, 99.999%), tin(II) iodide (SnI_2, 99%), tin(II) sulfate ($SnSO_4$, 95%), and bismuth(III) chloride ($BiCl_3$, 99%) from Strem; oleic acid (technical grade, 90%) from Alfa Aesar; hexanes (99.9%) and methanol (99.9%) from Fisher. All chemicals were used as received without further purification.

Synthesis of Thiocyanate Precursors. $Bi(SCN)_3$, $KSn(SO_4)$-SCN, and $Sn(SCN)_2$ were prepared according to the literature methods. *$Bi(SCN)_3$.* Inside a N_2-filled drybox, $BiCl_3$ (534 mg, 1.7 mmol), KSCN (576 mg, 4.7 mmol), and anhydrous THF (60 mL) were added to a round-bottom flask (R.B.) and stirred for 18 h at room temperature (R.T., 21 °C). After filtration to remove the formed precipitate (KCl), the supernatant was evaporated under vacuum to yield bright orange crystals (Yield: 0.291 g, 44%).[55] *$KSn(SO_4)SCN$.* A solution of $SnSO_4$ (4 g, 19 mmol) and concentrated H_2SO_4 (3 drops) in deionized water (25 mL) was filtered into a solution of KSCN (4 g, 41 mmol) in deionized water (12.5 mL). After sitting at 0 °C for 24 h, the white precipitate was collected by filtration, washed with deionized water, and dried over vacuum (Yield: 1.627 g, 27%).[56] *$Sn(SCN)_2$.* A solution of $SnSO_4$ (4 g, 19 mmol) and 1.0 M H_2SO_4 (4 mL) in deionized water (21 mL) was filtered into a solution of NaSCN (6 g, 74 mmol) in deionized water (25 mL). After 5 h at R.T., then the mixture was left for 5 h at 0 °C. White crystals were isolated by filtration, washed with deionized water, and dried under vacuum (Yield: 1.383 g, 31%).[57]

Synthesis of Chalcohalides. All syntheses were performed in air under standard ambient conditions. *Quaternaries: $Sn_2SbS_2I_3$.* A mixture of $Sn(SCN)_2$ (94 mg, 0.4 mmol), SbI_3 (100 mg, 0.2 mmol), ODE (8 mL, 25 mmol), and oleic acid (2 mL, 6.3 mmol) was stirred in a three-neck R.B. flask for ca. 5 min at 140 °C until all solids dissolved or suspended. The mixture was heated to 300 °C, allowed to sit for 30 s, and allowed to cool to R.T. by removing the heating mantle. *$Sn_2BiS_2I_3$.* Prepared in a similar manner using a mixture of $Sn(SCN)_2$ (94 mg, 0.4 mmol), BiI_3 (118 mg, 0.2 mmol), SnI_2 (75 mg, 0.2 mmol), ODE (8 mL, 25 mmol), and oleic acid (2 mL, 6.3 mmol). *Sn_2BiSI_5.* Prepared in a similar manner using a mixture of $Sn(SCN)_2$ (47 mg, 0.2 mmol), SnI_2 (0.4 or 0.6 mmol, see discussion), BiI_3 (118 mg, 0.2 mmol), ODE (2 mL, 6.3 mmol), and oleic acid (8 mL, 25 mmol). *Ternaries: $Sn_2SI_2(Pnma)$.* A mixture of $Sn(SCN)_2$ (47 mg, 0.2 mmol), SnI_2 (0.2, 0.4, or 0.6 mmol, see discussion) ODE (8 mL, 25 mmol), and oleic acid (2 mL, 6.3 mmol) was stirred in a three-neck R.B. flask at 140 °C until all solids dissolved or suspended. The mixture was heated to 300 °C for 30 s and allowed to cool to R.T. by removing the heating mantle. *$Sn_2SI_2(C2/m)$.* Prepared in a similar manner using SnI_2 (300 mg, 0.8 mmol), with OA (8 mL, 25 mmol) and ODE (2 mL, 6.3 mmol). *Purification.* Crude chalcohalide solutions were initially centrifuged at 4500 rpm for 5 min. After discarding the supernatant, the solids were resuspended in hexanes (5 mL), reprecipitated with methanol (5 mL) and centrifuged again. This process was repeated at least three times until the supernatant was colorless.

Optical Characterization. Diffuse-reflectance spectra were collected by using an SL1 Tungsten Halogen lamp (vis-IR), an SL3 Deuterium Lamp (UV), and a BLACK-Comet C-SR-100 spectrometer (200−1080 nm). Band gap values were estimated by extrapolating the linear slope of Tauc plots of $(Ah\nu)^r$ versus $h\nu$ (A = absorbance, $h\nu$ = incident photon energy in eV, with r = 1/2 for direct and r = 2 for indirect semiconductors).[61]

Structural Characterization. Powder X-ray diffraction (XRD) was measured on a Rigaku Ultima IV diffractometer (40 kV, 44 mA) using Cu K_α radiation on a zero-background quartz sample holder. Rietveld refinements were performed on XRD patterns using the GSAS-II software package.[79] Semiquantification of the binary, ternary, and quaternary phases observed in the XRD patterns were determined using the reference intensity ratio (RIR) method[80] applied within Match!.[81] Scanning electron microscopy (SEM) images were acquired on a JEOL JSM-IT200 scanning electron microscope.

Cyclic Voltammetry. Electrochemical studies were carried out using cyclic voltammetry (CV) with the potentiostat Workstation CHInstrumentAQ that was controlled by the software CHI660e V14.08. A three-electrode system and a thermostatic electrochemical cell were used for all of the measurements. Glassy carbon electrodes were used as the working (WE, 3 mm diameter) and counter (CE, 3 mm diameter) electrodes, and a saturated calomel electrode (SCE) was used as the reference electrode (RE). The working electrode was polished with 1 mm diamond paste (DP-Paste, P) and rinsed with ethanol after each set of measurements. The semiconductors were each dispersed in n-hexanes (1 mg/mL) followed by sonication for 1−2 min. Afterward, 50 μL of each sample was drop-cast onto the glassy carbon electrode surface, and the hexanes were fully evaporated. Prior to recording the CVs for the chalcohalides, blank experiments were conducted to ensure that the working electrode was polished and clean. No electrochemical signals were detected for nonmodified working electrodes in the selected potential range (from −2.5 to 1.5 V). CV experiments were performed under an inert atmosphere using the modified working electrode in a pure acetonitrile +0.1 M tetrabutylammonium hexafluoroborate (TBA BF_6) solution at different scan rates (ν = 0.1 to 0.7 V s^{-1}).

Solid-State ^{119}Sn NMR Spectroscopy. Solid-state NMR experiments were performed at two different fields (B_0 = 9.4 and 11.4 T). ^{119}Sn was referenced indirectly to ^{1}H in a mixture of tetramethylsilane in $CDCl_3$ and adamantane using IUPAC recommend frequencies.[82] NMR experiments at 9.4 T (400 MHz) were performed with a wide-bore magnet equipped with a Bruker AVANCE III HD console. NMR spectra were recorded on a 4.0 mm HXY MAS probe at a 12.5 kHz

https://doi.org/10.1021/acs.chemmater.4c00209
Chem. Mater. 2024, 36, 4542−4552

MAS. ^{119}Sn pulse length for $\pi/2$ and π pulses were 1.75 and 3.5 μs, respectively, corresponding to a 143 kHz RF field. Faster MAS frequencies was needed for experiments on Sn_2SI_2, thus a 2.5 mm HXY MAS probe was used. The ^{119}Sn pulse length for $\pi/2$ and π pulses were 1.92 and 3.84 μs respectively, corresponding to an ca. 130 kHz Rf field. Experiments at 14.1 T (600 MHz) were performed with a Bruker wide-bore magnet equipped with a Bruker AVANCE NEO console. Experiments were recorded on a 4.0 mm HXY MAS probe with 10 kHz MAS. $\pi/2$ and π pulse lengths were 3.02 and 6.04 μs, corresponding to an ca. 83 kHz Rf field. The ^{119}Sn NMR spectrum of Sn_2SI_2 was measured on a 2.5 mm HXY MAS probe with a pulse length of 1.96 and 3.92 μs for $\pi/2$ and π pulses. The ^{119}Sn Rf field was ca. 128 kHz. All experiments were performed with the probes configured in the double resonance (HX) mode to maximize sensitivity.

Thermal Analysis. TGA and DSC were carried out on chalcohalide samples (5−20 mg) using a Netzsch DSC/TGA (STA449 F1) and alumina (Al_2O_3) crucibles. The temperature program was a 10 °C/min ramp from 40−700 °C under either a nitrogen or air atmosphere.

Surface Characterization. X-ray photoelectron spectroscopy (XPS) was performed on a Kratos Amicus/ESCA3400 instrument. The samples of $Sn_2SbS_2I_3$ were irradiated with 240 W unmonochromated Mg K_α X-rays, and the energies of photoelectrons emitted at 0° from the surface were analyzed using a DuPont-type analyzer. The pass energy was set at 150 eV. CasaXPS was used to process the raw data files, and the binding energy of C 1s at 284.6 eV was used for reference.

■ ASSOCIATED CONTENT

Supporting Information

The Supporting Information is available free of charge at https://pubs.acs.org/doi/10.1021/acs.chemmater.4c00209.

Phase evolution plots, XRD, Rietveld refinements, SEM-EDS, diffuse reflectance, cyclic voltammograms, ssNMR, XPS, and TGA/DSC (PDF)

■ AUTHOR INFORMATION

Corresponding Author

Javier Vela − *Department of Chemistry, Iowa State University, Ames, Iowa 50011, United States; US DOE Ames National Laboratory, Ames, Iowa 50011, United States;* orcid.org/0000-0001-5124-6893; Email: vela@iastate.edu

Authors

Alison N. Roth − *Department of Chemistry, Iowa State University, Ames, Iowa 50011, United States; US DOE Ames National Laboratory, Ames, Iowa 50011, United States*

Andrew P. Porter − *Department of Chemistry, Iowa State University, Ames, Iowa 50011, United States; US DOE Ames National Laboratory, Ames, Iowa 50011, United States*

Sarah Horger − *Department of Chemistry, Iowa State University, Ames, Iowa 50011, United States*

Kerly Ochoa-Romero − *Departament de Química, Universitat Autònoma de Barcelona, Barcelona 08193, Spain*

Gonzalo Guirado − *Departament de Química, Universitat Autònoma de Barcelona, Barcelona 08193, Spain*

Aaron J. Rossini − *Department of Chemistry, Iowa State University, Ames, Iowa 50011, United States; US DOE Ames National Laboratory, Ames, Iowa 50011, United States;* orcid.org/0000-0002-1679-9203

Complete contact information is available at: https://pubs.acs.org/10.1021/acs.chemmater.4c00209

Notes

The authors declare no competing financial interest.

■ ACKNOWLEDGMENTS

We thank the U.S. National Science Foundation, Division of Chemistry, Macromolecular, Supramolecular, and Nanochemistry Program (2305062) for funding of this work. G.G. and K.O.-R. thank the European Union's Horizon Europe programme under grant agreement no. 101115182 (CONFETI—HORIZON-EIC-2022-PATHFINDERCHALLENGES-01) for financial support. A.P.P. and A.J.R. thank the U.S. Department of Energy (DOE), Materials Science and Engineering Division. Ames National Laboratory is operated for the U.S. DOE by Iowa State University, under contract no. DE-AC02-07CH11358. We also thank Dapeng Jing for assistance with XPS measurements.

■ REFERENCES

(1) Kamat, P. V.; Kuno, M. Halide Ion Migration in Perovskite Nanocrystals and Nanostructures. *Acc. Chem. Res.* **2021**, *54*, 520−531.

(2) Barker, A. J.; Sadhanala, A.; Deschler, F.; Gandini, M.; Senanayak, S. P.; Pearce, P. M.; Mosconi, E.; Pearson, A. J.; Wu, Y.; Kandada, A. R. S.; Leijtens, T.; De Angelis, F.; Dutton, S. E.; Petrozza, A.; Friend, R. H. Defect-Assisted Photoinduced Halide Segregation in Mixed-Halide Perovskite Thin Films. *ACS Energy Lett.* **2017**, *2*, 1416−1424.

(3) Kwak, J. I.; Nam, S. H.; Kim, L.; An, Y. J. Potential Environmental Risk of Solar Cells: Current Knowledge and Future Challenges. *J. Hazard. Mater.* **2020**, *392*, No. 122297.

(4) Su, P.; Liu, Y.; Zhang, J.; Chen, C.; Yang, B.; Zhang, C.; Zhao, X. Pb-Based Perovskite Solar Cells and the Underlying Pollution behind Clean Energy: Dynamic Leaching of Toxic Substances from Discarded Perovskite Solar Cells. *J. Phys. Chem. Lett.* **2020**, *11*, 2812−2817.

(5) Ni, Z.; Jiao, H.; Fei, C.; Gu, H.; Xu, S.; Yu, Z.; Yang, G.; Deng, Y.; Jiang, Q.; Liu, Y.; Yan, Y.; Huang, J. Evolution of Defects during the Degradation of Metal Halide Perovskite Solar Cells under Reverse Bias and Illumination. *Nat. Energy* **2022**, *7*, 65−73.

(6) Huang, Y. T.; Kavanagh, S. R.; Scanlon, D. O.; Walsh, A.; Hoye, R. L. Z. Perovskite-Inspired Materials for Photovoltaics and Beyond—From Design to Devices. *Nanotechnology* **2021**, *32*, 132004.

(7) Chen, M.; Dong, X.; Luo, W.; Fang, Z.; Shan, Z.; Liu, S.; Xu, Z. First-Principles Study of Quaternary Thioiodides for Stable Lead-Free Solar Cells. *J. Mater. Chem. C* **2023**, *11*, 10520−10526.

(8) Henkel, P.; Li, J.; Grandhi, G. K.; Vivo, P.; Rinke, P. Screening Mixed-Metal $Sn_2M(III)Ch_2X_3$ Chalcohalides for Photovoltaic Applications. *Chem. Mater.* **2023**, *35*, 7761−7769.

(9) Sebastiá-Luna, P.; Rodkey, N.; Mirza, A. S.; Mertens, S.; Lal, S.; Carranza, A. M. G.; Calbo, J.; Righetto, M.; Sessolo, M.; Herz, L. M.; Vandewal, K.; Ortí, E.; Morales-Masis, M.; Bolink, H. J.; Palazon, F. Chalcohalide Antiperovskite Thin Films with Visible Light Absorption and High Charge-Carrier Mobility Processed by Solvent-Free and Low-Temperature Methods. *Chem. Mater.* **2023**, *35*, 6482−6490.

(10) Quarta, D.; Toso, S.; Fieramosca, A.; Dominici, L.; Caliandro, R.; Moliterni, A.; Tobaldi, D. M.; Saleh, G.; Gushchina, I.; Brescia, R.; Prato, M.; Infante, I.; Cola, A.; Giannini, C.; Manna, L.; Gigli, G.; Giansante, C. Direct Band Gap Chalcohalide Semiconductors: Quaternary $AgBiSCl_2$ Nanocrystals. *Chem. Mater.* **2023**, *35*, 9900−9906.

(11) Ghorpade, U. V.; Suryawanshi, M. P.; Green, M. A.; Wu, T.; Hao, X.; Ryan, K. M. Emerging Chalcohalide Materials for Energy Applications. *Chem. Rev.* **2023**, *123*, 327−378.

(12) Palazon, F. Metal Chalcohalides: Next Generation Photovoltaic Materials? *Sol. RRL* **2022**, *6*, 2100829.

(13) Li, J.; Han, S. S.; Guo, S. P. Chalcohalides: A Rising Type of Second-Order Nonlinear Optical Materials. *Eur. J. Inorg. Chem.* **2022**, e202200419.
(14) Xiao, J. R.; Yang, S. H.; Feng, F.; Xue, H. G.; Guo, S. P. A Review of the Structural Chemistry and Physical Properties of Metal Chalcogenide Halides. *Coord. Chem. Rev.* **2017**, *347*, 23−47.
(15) Ganose, A. M.; Savory, C. N.; Scanlon, D. O. Beyond Methylammonium Lead Iodide: Prospects for the Emergent Field of ns^2 Containing Solar Absorbers. *Chem. Commun.* **2017**, *53*, 20−44.
(16) Doussier, C.; Moëlo, Y.; Léone, P.; Meerschaut, A.; Evain, M. Crystal Structure of $Pb_2SbS_2I_3$, and Re-Examination of the Crystal Chemistry within the Group of (Pb/Sn/Sb) Chalcogeno-Iodides. *Solid State Sci.* **2007**, *9*, 792−803.
(17) Islam, S. M.; Malliakas, C. D.; Sarma, D.; Maloney, D. C.; Stoumpos, C. C.; Kontsevoi, O. Y.; Freeman, A. J.; Kanatzidis, M. G. Direct Gap Semiconductors $Pb_2BiS_2I_3$, $Sn_2BiS_2I_3$, and Sn_2BiSI_5. *Chem. Mater.* **2016**, *28*, 7332−7343.
(18) Starosta, V. I.; Kroutil, J.; Benes, L. Preparation and Fundamental Physical Properties of $Sn_2SbS_2I_3$ and $Pb_2SbS_2I_3$ Compounds. *Cryst. Res. Technol.* **1990**, *25*, 1439−1442.
(19) He, J.; Hu, X.; Liu, Z.; Chen, W.; Longo, G. Prospect for Bismuth/Antimony Chalcohalides-Based Solar Cells. *Adv. Funct. Mater.* **2023**, 2306075.
(20) Shyamal, S.; Pradhan, N. Nanostructured Metal Chalcohalide Photocatalysts: Crystal Structures, Synthesis, and Applications. *ACS Energy Lett.* **2023**, *8*, 3902−3926.
(21) Nicolson, A.; Breternitz, J.; Kavanagh, S. R.; Tomm, Y.; Morita, K.; Squires, A. G.; Tovar, M.; Walsh, A.; Schorr, S.; Scanlon, D. O. Interplay of Static and Dynamic Disorder in the Mixed-Metal Chalcohalide $Sn_2SbS_2I_3$. *J. Am. Chem. Soc.* **2023**, *145*, 12509−12517.
(22) Kavanagh, S. R.; Savory, C. N.; Scanlon, D. O.; Walsh, A. Hidden Spontaneous Polarisation in the Chalcohalide Photovoltaic Absorber $Sn_2SbS_2I_3$. *Mater. Horiz.* **2021**, *8*, 2709−2716.
(23) Mark, J.; Zhang, W.; Maeda, K.; Yamamoto, T.; Kageyama, H.; Mori, T. Ultralow Thermal Conductivity in the Mixed-Anion Solid Solution $Sn_2SbS_{2-x}Se_xI_3$. *J. Mater. Chem. A* **2023**, *11*, 10213−10221.
(24) Kumar, M.; Sheoran, S.; Bhattacharya, S. Exploring Chalcohalide Perovskite-Inspired Materials ($Sn_2SbX_2I_3$; X = S or Se) for Optoelectronic and Spintronic Applications. *J. Phys. Chem. Lett.* **2023**, *14*, 10158−10165.
(25) Nie, R.; Lee, K. S.; Hu, M.; Paik, M. J.; Seok, S. I. Heteroleptic Tin-Antimony Sulfoiodide for Stable and Lead-Free Solar Cells. *Matter.* **2020**, *3*, 1701−1713.
(26) Pitaro, M.; Tekelenburg, E. K.; Shao, S.; Loi, M. A. Tin Halide Perovskites: From Fundamental Properties to Solar Cells. *Adv. Mater.* **2022**, *34*, 2105844.
(27) Dolgikh, V. A. Preparation of Single Crystals and Dielectric Properties of $Sn_2SbS_2I_3$ and $Pb_2SbS_2I_3$. *Izv. Akad. Nauk SSSR Neorg. Mater.* **1985**, *21*, 1215−1218.
(28) Olivier-Fourcade, J.; Jumas, J. C.; Maurin, M.; Philippot, E. A New Sulfoiodide of Tin and Antimony: Structure Investigation. *Z. Anorg. Allg. Chem.* **1980**, *468*, 91−98.
(29) Ibanez, A.; Jumas, J. C.; Olivier-Fourcade, J.; Philippot, E. Synthesis and Characterization of Antimony and Tin Chalcogenoiodides. *Chim. Informationsdienst* **1984**, *21*, 344−357.
(30) Yang, C.; Wang, Z.; He, G.; Zhang, H.; Liao, C. $Pb_2BiS_2I_3$ Nanowires for Use in Photodetectors. *ACS Appl. Nano Mater.* **2022**, *5*, 16033−16038.
(31) Quarta, D.; Toso, S.; Saleh, G.; Caliandro, R.; Moliterni, A.; Griesi, A.; Divitini, G.; Infante, I.; Gigli, G.; Giannini, C.; Manna, L.; Giansante, C. Mixed Valence of Bismuth in Hexagonal Chalcohalide Nanocrystals. *Chem. Mater.* **2023**, *35*, 1029−1036.
(32) Groom, R.; Jacobs, A.; Cepeda, M.; Drummey, R.; Latturner, S. E. $Bi_{13}S_{18}I_2$: (Re)discovery of a Subvalent Bismuth Compound Featuring $[Bi_2]^{4+}$Dimers Grown in Sulfur/Iodine Flux Mixtures. *Chem. Mater.* **2017**, *29*, 3314−3323.
(33) Quarta, D.; Toso, S.; Giannuzzi, R.; Caliandro, R.; Moliterni, A.; Saleh, G.; Capodilupo, A. L.; Debellis, D.; Prato, M.; Nobile, C.; Maiorano, V.; Infante, I.; Gigli, G.; Giannini, C.; Manna, L.; Giansante, C. Colloidal Bismuth Chalcohalide Nanocrystals. *Angew. Chem., Int. Ed.* **2022**, *61*, e202201747.
(34) Li, S.; Xu, L.; Kong, X.; Kusunose, T.; Tsurumachi, N.; Feng, Q. $Bi_{13}S_{18}X_2$-Based Solar Cells (X = Cl, Br, I): Photoelectric Behavior and Photovoltaic Performance. *Phys. Rev. Appl.* **2021**, *15*, No. 034040.
(35) Mistewicz, K.; Das, T. K.; Nowacki, B.; Smalcerz, A.; Kim, H. J.; Hajra, S.; Godzierz, M.; Masiuchok, O. Bismuth Sulfoiodide (BiSI) Nanorods: Synthesis, Characterization, and Photodetector Application. *Sci. Rep.* **2023**, *13*, 1−15.
(36) Wang, Y.; Dai, X.; Dong, C.; Guo, W.; Xu, Z.; Chen, Y.; Xiang, H.; Zhang, R. Engineering Electronic Band Structure of Binary Thermoelectric Nanocatalysts for Augmented Pyrocatalytic Tumor Nanotherapy. *Adv. Mater.* **2022**, *34*, e2106773.
(37) Lee, D. W.; Woo, H. Y.; Choi, Y.; Chung, H.; Paik, T. Tailoring Sizes and Compositions of Heavy Pnictogen Bismuth Thiohalide Nanorods and Nanowires Via Heat-Up Method. *CrystEngComm* **2023**, *25*, 1755−1762.
(38) Fenner, J. The Crystal Structure of Sn_4SI_6. *Z. Naturforsch.* **1978**, *33*, 479−481.
(39) Thevet, F.; Dung, N. H.; Dagron, C.; Flahaut, J. Contribution to the Study of the System Formed by Tin, Sulfur and Iodine. Highlighting the Two Varieties of the Stannous Iodosulfide Sn_2SI_2: Thermal Behavior and Structural Study. *J. Solid State Chem.* **1976**, *18*, 175−182.
(40) Chen, J.; Wang, G.; Wei, J.; Guo, Y. Effect of Sulfur Dopant Atoms on the Electronic Band Gap and Optical Properties of Tin Iodide. *Chem. Phys. Lett.* **2019**, *730*, 557−561.
(41) Akkerman, Q. A.; Martín-García, B.; Buha, J.; Almeida, G.; Toso, S.; Marras, S.; Bonaccorso, F.; Petralanda, U.; Infante, I.; Manna, L. Ultrathin Orthorhombic PbS Nanosheets. *Chem. Mater.* **2019**, *31*, 8145−8153.
(42) Toso, S.; Akkerman, Q. A.; Martín-García, B.; Prato, M.; Zito, J.; Infante, I.; Dang, Z.; Moliterni, A.; Giannini, C.; Bladt, E.; Lobato, I.; Ramade, J.; Bals, S.; Buha, J.; Spirito, D.; Mugnaioli, E.; Gemmi, M.; Manna, L. Nanocrystals of Lead Chalcohalides: A Series of Kinetically Trapped Metastable Nanostructures. *J. Am. Chem. Soc.* **2020**, *142*, 10198−10211.
(43) Roth, A. N.; Opare-Addo, J.; Gi, E.; Mena, S.; Guirado, G.; Schaller, R. D.; Smith, E. A.; Vela, J. Solution-Phase Synthesis and Photoluminescence of Quaternary Chalcohalide Semiconductors. *Chem. Mater.* **2023**, *35*, 2165−2172.
(44) Roth, A. N.; Chen, Y.; Santhiran, A.; Opare-Addo, J.; Gi, E.; Smith, E. A.; Rossini, A. J.; Vela, J. Designing Complex $Pb_3SBr_xI_{4-x}$ Chalcohalides: Tunable Emission Semiconductors through Halide-Mixing. *Chem. Sci.* **2023**, *14*, 12331−12338.
(45) Sperry, B. M.; Kukhta, N. A.; Huang, Y.; Luscombe, C. K. Ligand Decomposition during Nanoparticle Synthesis: Influence of Ligand Structure and Precursor Selection. *Chem. Mater.* **2023**, *35*, 570−583.
(46) Roth, A. N.; Chen, Y.; Adamson, M. A. S.; Gi, E.; Wagner, M.; Rossini, A. J.; Vela, J. Alkaline-Earth Chalcogenide Nanocrystals: Solution-Phase Synthesis, Surface Chemistry, and Stability. *ACS Nano* **2022**, *16*, 12024−12035.
(47) Just, J.; Sutter-Fella, C. M.; Lützenkirchen-Hecht, D.; Frahm, R.; Schorr, S.; Unold, T. Secondary Phases and their Influence on the Composition of the Kesterite Phase in CZTS and CZTSe Thin Films. *Phys. Chem. Chem. Phys.* **2016**, *18*, 15988−15994.
(48) Huang, Y.; Cohen, T. A.; Sperry, B. M.; Larson, H.; Nguyen, H. A.; Homer, M. K.; Dou, F. Y.; Jacoby, L. M.; Cossairt, B. M.; Gamelin, D. R.; Luscombe, C. K. Organic Building Blocks at Inorganic Nanomaterial Interfaces. *Mater. Horiz.* **2022**, *9*, 61−87.
(49) Adamson, M. A. S.; Yox, P.; Hernandez, T.; Wang, F.; Vela, J. Phase Evolution, Polymorphism, and Catalytic Activity of Nickel Dichalcogenide Nanocrystals. *Chem. Mater.* **2022**, *34*, 746−755.
(50) White, M. A.; Baumler, K. J.; Chen, Y.; Venkatesh, A.; Medina-Gonzalez, A. M.; Rossini, A. J.; Zaikina, J. V.; Chan, E. M.; Vela, J. Expanding the I−II−V Phase Space: Soft Synthesis of Polytypic Ternary and Binary Zinc Antimonides. *Chem. Mater.* **2018**, *30*, 6173−6182.

https://doi.org/10.1021/acs.chemmater.4c00209
Chem. Mater. 2024, 36, 4542−4552

(51) Rosales, B. A.; White, M. A.; Vela, J. Solution-Grown Sodium Bismuth Dichalcogenides: Toward Earth-Abundant, Biocompatible Semiconductors. *J. Am. Chem. Soc.* **2018**, *140*, 3736−3742.
(52) Tappan, B. A.; Horton, M. K.; Brutchey, R. L. Ligand-Mediated Phase Control in Colloidal $AgInSe_2$ Nanocrystals. *Chem. Mater.* **2020**, *32*, 2935−2945.
(53) Tappan, B. A.; Barim, G.; Kwok, J. C.; Brutchey, R. L. Utilizing Diselenide Precursors toward Rationally Controlled Synthesis of Metastable $CuInSe_2$ Nanocrystals. *Chem. Mater.* **2018**, *30*, 5704−5713.
(54) Tappan, B. A.; Brutchey, R. L. Polymorphic Metastability in Colloidal Semiconductor Nanocrystals. *ChemNanoMat* **2020**, *6*, 1567−1588.
(55) Crispini, A.; Errington, R. J.; Fisher, G. A.; Funke, F. J.; Norman, N. C.; Orpen, A. G.; Stratford, S. E.; Struve, O. Synthetic and Structural Studies on Bismuth(III) Thiocyanate and Selenocyanate Complexes. *J. Chem. Soc., Dalton Trans.* **1994**, *9*, 1327−1335.
(56) Chamberlain, B. R.; Moser, W. Tin(II) Thiocyanate and Complex Thiocyanates. *J. Chem. Soc. A* **1969**, 354−358, DOI: 10.1039/J19690000354.
(57) Wechwithayakhlung, C.; Packwood, D. M.; Chaopaknam, J.; Worakajit, P.; Ittisanronnachai, S.; Chanlek, N.; Promarak, V.; Kongpatpanich, K.; Harding, D. J.; Pattanasattayavong, P. Tin(II) Thiocyanate $Sn(NCS)_2$ − A Wide Band Gap Coordination Polymer Semiconductor with a 2D Structure. *J. Mater. Chem. C* **2019**, *7*, 3452−3462.
(58) Akkerman, Q. A.; Martínez-Sarti, L.; Goldoni, L.; Imran, M.; Baranov, D.; Bolink, H. J.; Palazon, F.; Manna, L. Molecular Iodine for a General Synthesis of Binary and Ternary Inorganic and Hybrid Organic−Inorganic Iodide Nanocrystals. *Chem. Mater.* **2018**, *30*, 6915−6921.
(59) Haynes, W. M.; Lide, D. R.; Bruno, T. J. *CRC Handbook of Chemistry and Physics*, 103rd ed., CRC Press: Boca Raton, FL, 2022.
(60) Hammond, G. S. A Correlation of Reaction Rates. *J. Am. Chem. Soc.* **1955**, *77*, 334−338.
(61) Viezbicke, B. D.; Patel, S.; Davis, B. E.; Birnie, D. P. Evaluation of the Tauc Method for Optical Absorption Edge Determination: ZnO Thin Films as a Model System. *Phys. Status Solidi B* **2015**, *252*, 1700−1710.
(62) *Multinuclear Solid-State NMR of Inorganic Materials*, 1st ed. In Pergamon Materials Series; MacKenzie, K. J. D.; Smith, M. E., Eds.; Vol. *6*; Pergamon, 2002; pp 3−727. ISBN: 978−0-08−043787−3.
(63) Kubicki, D. J.; Prochowicz, D.; Salager, S.; Rakhmatullin, A.; Grey, C. P.; Emsley, L.; Stranks, S. D. Local Structure and Dynamics in Methylammonium, Formamidinium, and Cesium Tin(II) Mixed-Halide Perovskites from ^{119}Sn Solid-State NMR. *J. Am. Chem. Soc.* **2020**, *142*, 7813−7826.
(64) Pietrass, T.; Taulelle, F. ^{119}Sn Solid-State NMR of Tin Sulfides. Evidence of Polytypism in SnS_2. *Magn. Reson. Chem.* **1997**, *35*, 363−366.
(65) Kofod, P. Lineshapes of a Spin-1/2 Nucleus with Scalar Coupling to a Quadrupolar Nucleus Subject to Random Field Relaxation. *J. Magn. Reson., Ser. A* **1996**, *119*, 219−224.
(66) Sharp, R. R. Field Dependence of Nuclear Magnetic Relaxation of ^{119}Sn in $SnCl_4$, $SnBr_4$, and SnI_4. *J. Chem. Phys.* **1974**, *60*, 1149−1157.
(67) Protesescu, L.; Yakunin, S.; Bodnarchuk, M. I.; Krieg, F.; Caputo, R.; Hendon, C. H.; Yang, R. X.; Walsh, A.; Kovalenko, M. V. Nanocrystals of Cesium Lead Halide Perovskites ($CsPbX_3$, X = Cl, Br, and I): Novel Optoelectronic Materials Showing Bright Emission with Wide Color Gamut. *Nano Lett.* **2015**, *15*, 3692−3696.
(68) Jellicoe, T. C.; Richter, J. M.; Glass, H. F. J.; Tabachnyk, M.; Brady, R.; Dutton, S. E.; Rao, A.; Friend, R. H.; Credgington, D.; Greenham, N. C.; Böhm, M. L. Synthesis and Optical Properties of Lead-Free Cesium Tin Halide Perovskite Nanocrystals. *J. Am. Chem. Soc.* **2016**, *138*, 2941−2944.
(69) Naumkin, A. V.; Kraut-Vass, A.; Gaarenstroom, S. W.; Powell, C. J. *NIST X-ray Photoelectron Spectroscopy Database. NIST Standard Reference Database 20*, version 4.1; Measurement Services Division of the National Institute of Standards and Technology (NIST) Material Measurement Laboratory (MML), 2012. https://srdata.nist.gov/xps/.
(70) Boote, B. W.; Andaraarachchi, H. P.; Rosales, B. A.; Blome-Fernández, R.; Zhu, F.; Reichert, M. D.; Santra, K.; Li, J.; Petrich, J. W.; Vela, J.; Smith, E. A. Unveiling the Photo- and Thermal-Stability of Cesium Lead Halide Perovskite Nanocrystals. *ChemPhysChem* **2019**, *20*, 2647−2656.
(71) Han, X.; Liang, J.; Yang, J.; Soni, K.; Fang, Q.; Wang, W.; Zhang, J.; Jia, S.; Martí, A. A.; Zhao, Y.; Lou, J. Lead-Free Double Perovskite Cs_2SnX_6: Facile Solution Synthesis and Excellent Stability. *Small* **2019**, *15*, 1901650.
(72) Jiang, Y.; Zhang, H.; Qiu, X.; Cao, B. The Air and Thermal Stabilities of Lead-Free Perovskite Variant Cs_2SnI_6 Powder. *Mater. Lett.* **2017**, *199*, 50−52.
(73) Ju, D.; Dang, Y.; Zhu, Z.; Liu, H.; Chueh, C. C.; Li, X.; Wang, L.; Hu, X.; Jen, A. K. Y.; Tao, X. Tunable Band Gap and Long Carrier Recombination Lifetime of Stable Mixed $CH_3NH_3Pb_xSn_{1-x}Br_3$ Single Crystals. *Chem. Mater.* **2018**, *30*, 1556−1565.
(74) Hoffman, J. B.; Zaiats, G.; Wappes, I.; Kamat, P. V. $CsPbBr_3$ Solar Cells: Controlled Film Growth through Layer-by-Layer Quantum Dot Deposition. *Chem. Mater.* **2017**, *29*, 9767−9774.
(75) Wu, C.; Guo, D.; Li, P.; Wang, S.; Liu, A.; Wu, F. A Study on the Effects of Mixed Organic Cations on the Structure and Properties in Lead Halide Perovskites. *Phys. Chem. Chem. Phys.* **2020**, *22*, 3105−3111.
(76) Leijtens, T.; Prasanna, R.; Gold-Parker, A.; Toney, M. F.; McGehee, M. D. Mechanism of Tin Oxidation and Stabilization by Lead Substitution in Tin Halide Perovskites. *ACS Energy Lett.* **2017**, *2*, 2159−2165.
(77) Li, X. H.; Shi, Z. H.; Yang, M.; Liu, W.; Guo, S. P. $Sn_7Br_{10}S_2$: The First Ternary Halogen-Rich Chalcohalide Exhibiting a Chiral Structure and Pronounced Nonlinear Optical Properties. *Angew. Chem., Int. Ed.* **2022**, *61*, e202115871.
(78) Ran, M. Y.; Zhou, S. H.; Wei, W.; Song, B. J.; Shi, Y. F.; Wu, X. T.; Lin, H.; Zhu, Q. L. Quaternary Chalcohalides $CdSnSX_2$ (X = Cl or Br) with Neutral Layers: Syntheses, Structures, and Photocatalytic Properties. *Inorg. Chem.* **2021**, *60*, 3431−3438.
(79) Toby, B. H.; Von Dreele, R. B. GSAS-II: The Genesis of a Modern Open-Source All Purpose Crystallography Software Package. *J. Appl. Crystallogr.* **2013**, *46*, 544−549.
(80) Visser, J. W.; De Wolff, P. M. *Absolute Intensities*. Report 641.109, Technisch Physische Dienst: Delft, Netherlands, 1964.
(81) Putz, H.; Brandenburg, K. *Match! Version 3.11.5.203 (64-bit)*; Crystal Impact: Bonn, Germany, 2021, https://www.crystalimpact.de/match.
(82) Harris, R. K.; Becker, E. D.; de Menezes, S. M. C.; Goodfellow, R.; Granger, P. NMR Nomenclature: Nuclear Spin Properties and Conventions for Chemical Shifts. IUPAC Recommendations 2001. *Solid State Nucl. Magn. Reson.* **2002**, *22*, 458−483.

https://doi.org/10.1021/acs.chemmater.4c00209
Chem. Mater. 2024, 36, 4542−4552